Nonlinear Modeling and Stability Analysis of Grid-Tied Paralleled-Converters Systems Based on the Proposed Dual-Iterative Equal Area Criterion

Xilin Li, *Student Member, IEEE*, Zhen Tian, *Member, IEEE*, Xiaoming Zha, *Senior Member, IEEE*, Pengfei Sun, Yufei Hu, Meng Huang, *Member, IEEE*, and Jianjun Sun, *Member, IEEE*

***Abstract*—With the rapid development of distributed renewable energy generation and integration, stability issues of power converters systems have been widely studied in recent years. Many previous studies focus on the transient stability of a single converter connected to the weak grid. However, the nonlinear dynamics and stability mechanism of multiple converters systems remain unclear. In this article, a unified nonlinear model of the paralleled-converters system is established, which reveals the interactive power and interactive damping among multiple converters and the weak grid. To analyze the impacts of the interactive power and damping terms on system stability, a dual-iterative equal area criterion (DITEAC) is proposed with a dual-layer iterative calculation of the accelerating area and decelerating area. Compared with the previous studies, the proposed DITEAC method could deal with the nonlinear interactive damping and reduce the conservatism caused by the inequality scaling, which greatly improves the calculation accuracy of stability boundaries. The expansion feasibility of the proposed unified nonlinear model and DITEAC method to the *N*-converters system is fully discussed. Eventually, simulation and hardware-in-loop experiment results are presented to verify the effectiveness of the proposed method.**

***Index Terms*—Dual-iterative equal area criterion (DITEAC), grid-tied converters, nonlinear damping, nonlinear interaction, transient stability.**

I. Introduction

With the increasing popularity of renewable energy generators, converter-dominated power systems have received increasing attention in recent years [1], [2], [3]. There are two main types of grid-connected converters: grid-forming converters (GFM-VSCs) and grid-following converters (GFL-VSCs) [4], [5], [6]. Compared with the GFM-VSCs, the GFL-VSCs are more prone to lose stability under severe grid faults due to the low inertia characteristic. The converter instability generally causes the renewable energy generators to trip off the grid, seriously threatening the system's safe and stable operation [7]. Therefore, the stability analysis of GFL-VSCs is of great interest to academic and industrial peers.

The phase-locked loop (PLL) is commonly adopted for the GFL-VSCs to achieve synchronization with the grid, which has a great impact on the transient stability of the GFL-VSCs [8]. Small signal analysis has been widely conducted with linear models by various methods. The impedance-based modeling and generalized Nyquist criterion of the grid-connected VSCs are proposed in [9]. Other small-signal methods, such as eigenvalue analysis, have also been extensively studied [10], [11], [12]. However, these small-signal stability analysis methods are not applicable to the system under large-signal disturbance since the operation points are varying.

Several methods have been reported for the large-signal stability analysis of the converter system. In [13], a second-order nonlinear model of GFL-VSC connected to the weak grid system is built, and the equal area criterion (EAC) is adopted for transient stability. However, due to ignoring the adverse effect of the nonlinear damping, the derived stability region is larger than the actual one, which may misjudge an unstable system to be stable. In [14], a Hamilton-based method is proposed for the converter system's modeling and synchronization stability analysis, which renders an explicit stability criterion and attraction region estimation from the energy perspective. Besides, a Lyapunov-based method is applied for the stability analysis of a single converter system [15]. However, these above-mentioned methods are inevitably conservative because the region of negative damping is completely neglected, which indicates these stability criteria are only effective when the nonlinear damping is positive. To deal with the nonlinear damping, an improved equal area criterion (IEAC) is proposed in [16] with an approximate calculation of the extra accelerating area caused by the negative damping, which could greatly reduce the conservatism compared with the Lyapunov methods. However, the conservatism of the IEAC cannot be completely eliminated due to ignorance of the positive damping and the errors caused by the approximate calculation.

Manuscript received 25 October 2022; revised 12 January 2023 and 8 February 2023; accepted 11 February 2023. Date of publication 20 February 2023; date of current version 20 April 2023. This work was supported in part by the National Key Research and Development Program of China under Grant 2022YFB2402701 and in part by the National Natural Science Foundation of China under Grants 52007134 and 52222707. Recommended for publication by Associate Editor F. J. Azcondo. *(Corresponding author: Zhen Tian.)*

The authors are with the School of Electrical Engineering and Automation, Wuhan University, Wuhan 430072, China, and also with the Key Laboratory of Integrated Energy Power Equipment and System Security, Hubei Province 430072, China (e-mail: snplee@whu.edu.cn; ztian.ee@whu.edu.cn; xmzha@whu.edu.cn; hitsunpf@163.com; hyf_keeprunning@163.com; meng.huang@whu.edu.cn; jjsun@whu.edu.cn).

Color versions of one or more figures in this article are available at https://doi.org/10.1109/TPEL.2023.3246763.

Digital Object Identifier 10.1109/TPEL.2023.3246763

The work in [17] and [18] analyze the influence of different control parameters on transient synchronization stability by solving the swing equation of PLL by phase portrait approach and approximation solution, respectively. However, most previous studies mainly focus on single-converter systems [19], which cannot be easily extended to multiple-converters systems.

Due to the nonlinear interactions among multiple converters and the weak grid, the dynamic modeling and transient stability analysis of paralleled-converters systems become much more complicated. As far, only several studies have been reported for the transient stability of multiple converters. In [20], the transient stability of paralleled current-controlled VSC and virtual synchronous generators is investigated by the extended EAC method. In [21] and [22], the transient stability of the paralleled converters system is investigated by the EAC method. However, the damping effect is ignored and the quantitative transient stability criterion considering the dynamic interaction between the converters is not given. A quantitative transient stability criterion is proposed in [23], based on the boundedness of trigonometric functions to scale the dynamic interactive electromagnetic power terms. However, the method earlier is still conservative to give an accurate estimation of the stable boundary. And [23] directly ignores the adverse impacts of the negative damping terms on system stability, which may cause misjudgment. Besides, most of the previous studies ignored the line impedance fluctuation caused by line frequency variation and adopted a constant impedance model. Although this can make the model simpler, it ignores the interaction between the grid dynamics and the converter dynamics, which makes the model less accurate and may cause misjudgment of the transient stability since it shows a smaller mechanical power.

Compared with the previous studies, the novelty of this article is summarized as follows:

1) A unified nonlinear model of the paralleled-converters system considering the line impedance fluctuation caused by line frequency variation is established based on the partial linearization technique [24], which preserves the body characteristics of the system and is applicable for transient stability analysis and nonlinear controller optimization.
2) To deal with the nonlinear interactive power and mutual damping, a dual-iterative equal area criterion (DITEAC) is proposed to derive stability boundaries of multiple converters' virtual power angles, which owns high accuracy and high efficiency.
3) The effects of both positive damping and negative damping are quantitatively analyzed, which renders a more accurate calculation of the accelerating and decelerating area to greatly reduce conservatism.

The rest of this article is organized as follows. Section II derives a unified nonlinear model of the paralleled-converters system considering the frequency fluctuation. In Section III, the nonintegrable interaction terms are handled to make them applicable for transient stability analysis. In Section IV, details of the proposed dual-iteration EAC method are given. Simulation and experimental results are presented in Section V to verify the effectiveness and superiority of the proposed method. Furthermore, the extension feasibility of the proposed method to the N-converters system is discussed in Section VI. The concluding remarks is given in Section VII.

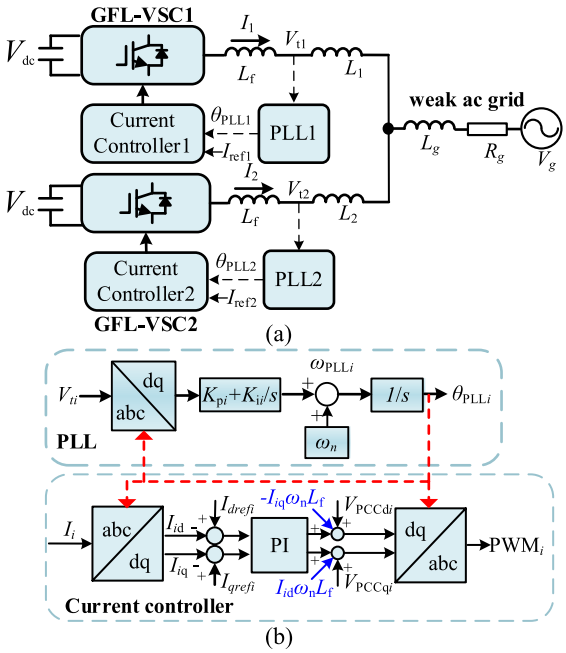

Fig. 1. Structure and control block of the paralleled-converters system.

II. Unified Nonlinear Modeling of Paralleled-Converters System

The structure of a simplified system with two paralleled converters is shown in Fig. 1. The converter VSC$_i$ ($i = 1, 2$) is connected to the weak grid through the grid inductance L_g and resistance R_g. L_i and I_i denote the line inductance and output current of the converter VSC$_i$, respectively. The control system of the converter contains a current control loop and a PLL. The conventional synchronous reference frame (SRF) PLL is displayed in Fig. 1(b). The SRF-PLL achieves synchronization with the grid by tracking the q-axis component of V_{ti} (VSC$_i$'s terminal voltage) V_{tiq}. K_{pi} and K_{ii} denote the proportional and integral gain of the PI controller parameters of the SRF-PLL, respectively. θ_{PLLi} and ω_{PLLi} denote the output angle and frequency of the PLL, respectively. θ_g and ω_g denote the angle and frequency of the grid voltage V_g. It is assumed that the grid frequency is constant such that $\omega_g = \omega_n$, where ω_n is the nominal grid frequency.

According to [14], the dynamics of the current control loop are much faster than that of PLL. Therefore, to simplify the synchronization analysis, the output current's amplitude I_i is assumed to be equal to its reference value I_{refi}.

According to Kirchhoff's voltage law, there is

$$V_{t1}\angle\theta_{t1} = V_g\angle\theta_g + I_1(R_g + R_1)\angle(\theta_{PLL1} + \varphi_1) + I_2R_g\angle(\theta_{PLL2} + \varphi_2)$$

$$
\begin{aligned}
&+(L_g+L_1)\frac{dI_1\angle(\theta_{\mathrm{PLL1}}+\varphi_1)}{dt}\\
&+L_g\frac{dI_2\angle(\theta_{\mathrm{PLL2}}+\varphi_2)}{dt}\\
V_{\mathrm{t2}}\angle\theta_{\mathrm{t2}} &= V_g\angle\theta_g+I_2(R_g+R_2)\angle(\theta_{\mathrm{PLL2}}+\varphi_2)\\
&+I_1R_g\angle(\theta_{\mathrm{PLL1}}+\varphi_1)\\
&+(L_g+L_2)\frac{dI_2\angle(\theta_{\mathrm{PLL2}}+\varphi_2)}{dt}\\
&+L_g\frac{dI_1\angle(\theta_{\mathrm{PLL1}}+\varphi_1)}{dt} \qquad (1)
\end{aligned}
$$

where $\varphi_i=\arctan(I_{i\mathrm{q}}/I_{i\mathrm{d}})$ denotes the angle difference between I_i and $\theta_{\mathrm{PLL}i}$. $I_{i\mathrm{d}}$ and $I_{i\mathrm{q}}$ are d- and q-axis components of I_i. When the converter is operated under the unity power factor condition, φ_i is set to 0. Applying the Park transformation with the reference angle $\theta_{\mathrm{PLL}i}$, the q-axis voltage of $V_{\mathrm{t}i}$ can be derived as follows:

$$
\begin{aligned}
&V_{\mathrm{t1q}}=V_{\mathrm{g}}\sin(\theta_{\mathrm{g}}-\theta_{\mathrm{PLL1}})+I_2R_{\mathrm{g}}\sin(\theta_{\mathrm{PLL2}}-\theta_{\mathrm{PLL1}})\\
&+\omega_{\mathrm{PLL1}}I_1(L_{\mathrm{g}}+L_1)+\omega_{PLL2}I_2L_{\mathrm{g}}\cos(\theta_{\mathrm{PLL2}}-\theta_{PLL1})\\
&V_{\mathrm{t2q}}=V_{\mathrm{g}}\sin(\theta_{\mathrm{g}}-\theta_{\mathrm{PLL2}})+I_1R_g\sin(\theta_{\mathrm{PLL1}}-\theta_{\mathrm{PLL2}})\\
&+\omega_{\mathrm{PLL2}}I_2\left(L_g+L_2\right)+\omega_{\mathrm{PLL1}}I_1L_{\mathrm{g}}\cos(\theta_{\mathrm{PLL1}}-\theta_{\mathrm{PLL2}}). \qquad (2)
\end{aligned}
$$

According to Fig. 1, the dynamics of PLL can be written as follows:

$$
\theta_{\mathrm{PLL}i}=\int_0^t\left[\omega_{\mathrm{n}}+K_{\mathrm{p}i}V_{tiq}+K_{\mathrm{i}i}\int_0^tV_{tiq}\mathrm{d}\tau\right]\mathrm{d}\tau. \qquad (3)
$$

Define $\delta_i=\theta_{\mathrm{PLL}i}-\theta_{\mathrm{g}}$ and $\omega_i=\mathrm{d}\delta_i/\mathrm{d}t$ as the virtual power angle and frequency of VSC$_i$, respectively. Combining (2) and (3), the dynamics of the paralleled-converters system can be derived as follows:

$$
\begin{aligned}
M_1\delta''_1 &= \underbrace{a_0}_{P_{\mathrm{M}}}-\underbrace{a_1\sin(\delta_1)}_{P_{\mathrm{E}}}\underbrace{-a_2\sin(\delta_2)-a_3\sin(\delta_{12}+\varphi_{\mathrm{E1}})}_{P_{\mathrm{int1}}(\delta_1,\delta_2)}\\
&-\underbrace{(a_4+a_5\cos(\delta_1)+a_6\cos(\delta_{12}+\varphi_{\mathrm{D11}}))}_{D_{\mathrm{s1}}(\delta_1,\delta_2)}\omega_1\\
&-\underbrace{(a_7+a_8\cos(\delta_2)+a_9\cos(\delta_{21}+\varphi_{\mathrm{D12}}))}_{D_{\mathrm{m1}}(\delta_1,\delta_2)}\omega_2 \qquad (4)
\end{aligned}
$$

where M_1 denotes the equivalent inertia coefficient of VSC$_1$. a_0 represents the mechanical power (P_{M}) of VSC$_1$, $a_1\sin\delta_1$ represents the electromagnetic power (P_{E}) between VSC$_1$&grid; $P_{\mathrm{int1}}(\delta_1,\ \delta_2)=a_2\sin\delta_2+a_3\sin(\delta_{12}+\varphi_{\mathrm{E1}})$ represents the interactive electromagnetic power between VSC$_2$&grid and VSC$_1$&VSC$_2$. The self-damping D_{s1} acts on the frequency ω_1 of VSC$_1$ itself, containing three parts: (1) $a_4\cos(\theta_1-\theta_1)$: performed by VSC$_1$; (2) $a_5\cos(\theta_1-\theta_{\mathrm{g}})$: performed by the grid; and (3) $a_6\cos(\theta_1-\theta_2+\varphi_{\mathrm{D11}})$: performed by VSC$_2$. Similarly, the mutual-damping D_{m1} acts on the frequency ω_2 of VSC$_2$, containing: (1) $a_7\cos(\theta_2-\theta_2)$: performed by the VSC$_2$; (2) $a_8\cos(\theta_2-\theta_{\mathrm{g}})$: performed by the grid; and (3) $a_9\cos(\theta_2-\theta_1+\varphi_{\mathrm{D12}})$: performed by VSC$_1$. The expression and physical meaning of VSC$_2$'s dynamics can be derived by replacing a_i with b_i, respectively. Specific expressions of these model coefficients: M_i, a_i, and b_i are given in Appendix A.

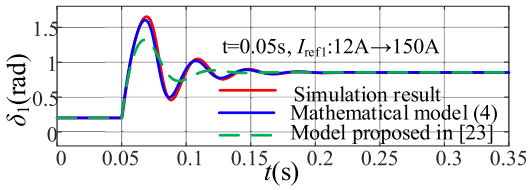

Fig. 2. Model validation of (4) under large disturbance.

Compared with conventional modeling with constant grid impedance in [23], the established model (4) captures the main nonlinear and interactive dynamics of the paralleled-converters system with higher accuracy. As shown in Fig. 2, the simulation result illustrates that the model error of (4) is relatively small and acceptable for stability analysis. The acceptable error of (4) is mainly caused by the dynamics of the current loop. The conventional model in [23] shows a smaller P_{M} due to the ignorance of frequency fluctuation on the grid, which leads to a smaller accelerating area and a larger maximum decelerating area compared with the real system. Therefore, the Conventional model [23] may misjudge an unstable system to be stable, which is unacceptable in the practical application.

III. Inequality Scaling of the Interactive Terms for Stability Analysis

For conventional SGs, the power angle δ_{ij} is only driven by the electromagnetic power exchanged between SG$_i$&SG$_j$. However, for the converters with PLLs, the dynamics of δ_i are coupled to each other due to the voltage drop at $V_{\mathrm{t}iq}$ on the grid impedance, as shown in (2) and (4). The interactive characteristics of the paralleled-converters system make it more complicated for stability analysis. $P_{\mathrm{int1}}(\delta_1,\ \delta_2)$, $\omega_1D_{\mathrm{s1}}(\delta_1,\ \delta_2)$, and $\omega_2D_{\mathrm{m1}}(\delta_1,\ \delta_2)$ are collectively referred to as interaction terms. This section mainly analyzes the impacts of the interaction terms and simplifies them for the application of the proposed dual-iterative EAC.

The EAC methods have been widely applied in synchronization stability analysis. However, EAC is a second-order method and cannot directly handle the nonintegrable interaction terms coupled in (4). Therefore, to extend the EAC method, inequality scaling is needed to assess the most adverse effects of interaction terms on system stability, which is also to prevent misjudgment [23]. The interaction terms are thus simplified to be determined only by the local power angle and frequency. Therefore, the EAC method can be skillfully extended to the transient stability analysis of the paralleled-converters system. Although the scaling process may bring conservatism to the stability analysis results.

A. Scaling of the Interactive Electromagnetic Power Terms

Based on the derivation in Appendix A, there are $0<a_2<a_3\ll a_0<a_1$. To prevent misjudgment, the most adverse effect of

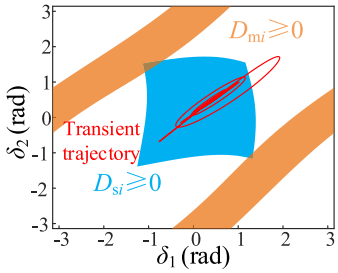

Fig. 3. Positive region of self-damping and mutual-damping.

the interactive electromagnetic power $P_{\mathrm{int}\,i}$ should be considered by scaling it to the minimum through the inequality scaling as follows:

$$\begin{cases} P_{\mathrm{int1}}(\delta_1,\delta_2) \geq a_2\sin(\delta_2) - a_3 \geq a_2\sin(\delta_{2\,\min}) \\ -a_3 = P_{\mathrm{int1\_min}} \\ P_{\mathrm{int2}}(\delta_1,\delta_2) \geq b_2\sin(\delta_1) \\ -b_3 \geq b_2\sin(\delta_{1\,\min}) - b_3 = P_{\mathrm{int2\_min}} \end{cases} \tag{5}$$

where $\delta_{i\min}$ is the lower boundary of VSC$_i$. The scaling process in (5) determines the boundary of δ_i based on EAC theory, while (5) is also determined by the δ_i' s boundary in return. Therefore, an iteration method is naturally proposed in the following section to reduce the conservatism caused by the inequality scaling in (5).

B. Discussion of Positive and Negative Damping Region

Both of $D_{\mathrm{s}\,i}$ and $D_{\mathrm{m}\,i}$ are nonlinear and vary with power angles, as shown in Fig. 3. The blue part denotes the positive region of $D_{\mathrm{s}\,i}$, while the orange part denotes the positive region of $D_{\mathrm{m}\,i}$. It is seen that both damping terms may exhibit negative characteristics during the transient process (the red solid curve). The negative damping will impose energy on the system, which is equivalent to increasing P_{M} [16]. Therefore, the varying damping impacts should be fully captured due to their adverse impacts on stability [16]. The stability criterion proposed in [23] directly ignores the varying damping, which leads to the risk of stability misjudgment.

C. Scaling of the Nonlinear Damping Terms

Although the damping terms have great impacts on the stability of the paralleled-converters system, the quantitative estimation of the work done by the damping terms is rarely studied, since the interactive damping terms in (4) are nonintegrable. Therefore, a similar scaling process needs to be conducted to convert the nonintegrable damping terms to integrable ones. To avoid misjudgment of stability, the energy imposed on the system by the negative damping terms needs to be scaled to their maximum values [16]. According to Appendix A: a_7, b_7, a_9, and b_9 are negative, while a_8 and b_8 are positive. Therefore, the mutual damping terms $D_{\mathrm{m}\,i}$ can be scaled to $D_{\mathrm{m}\,i\_\min}$

$$\begin{cases} D_{\mathrm{m1}}(\delta_1,\delta_2) > a_7 + a_8\cos\delta_{2\max} + a_9 = D_{\mathrm{m1\_min}}(\delta_{2\max}) \\ D_{\mathrm{m2}}(\delta_1,\delta_2) > b_7 + b_8\cos\delta_{1\max} + b_9 = D_{\mathrm{m2\_min}}(\delta_{1\max}) \end{cases}. \tag{6}$$

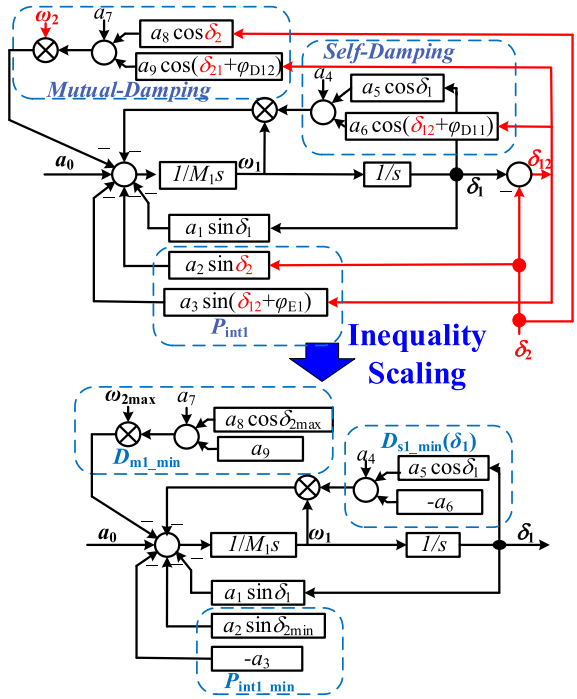

Fig. 4. Schematic diagram of the proposed scaling process.

However, $\omega_k D_{\mathrm{m}\,i\_\min}$ is still nonintegrable unless a mapping function $\omega_k(\delta_i)$ from δ_i to ω_k can be derived. This is impossible because the high-order nonlinear differential (4) cannot be solved explicitly in the time domain. Enlightened by the IEAC proposed in [16], the work done by $D_{\mathrm{m}\,i\_\min}$ can be further scaled with the maximum value of ω_k

$$\begin{cases} \int D_{\mathrm{m1}}(\delta_1,\delta_2)\omega_2 \mathrm{d}\delta_1 > \int D_{\mathrm{m1\_min}}\omega_{2\max}\mathrm{d}\delta_1 \\ \int D_{\mathrm{m2}}(\delta_1,\delta_2)\omega_1 \mathrm{d}\delta_2 > \int D_{\mathrm{m2\_min}}\omega_{1\max}\mathrm{d}\delta_2 \end{cases} \tag{7}$$

where $\omega_{i\max}$ is the maximum frequency of the VSC$_i$

$$\begin{cases} 0.5M_1\omega_{1\max}^2 = \int_{\delta_{1e}}^{\delta_{1\max}} [P_{\mathrm{int1\_min}} + a_1\sin\delta_1 - a_0]\mathrm{d}\delta_1 \\ 0.5M_2\omega_{2\max}^2 = \int_{\delta_{2e}}^{\delta_{2\max}} [P_{\mathrm{int2\_min}} + b_1\sin\delta_2 - b_0]\mathrm{d}\delta_2 \end{cases} \tag{8}$$

where $\delta_{i\mathrm{e}}$ is the stable equilibrium point of (4).

A similar inequality scaling process can be conducted with the self-damping terms $D_{\mathrm{s}\,i}$. According to Appendix A, a_4 and b_4 are negative, while a_5, b_5, a_6, and b_6 are positive. Therefore, $D_{\mathrm{s}\,i}$ can be scaled to $D_{\mathrm{s}\,i\_\min}(\delta_i)$, as follows:

$$\begin{cases} D_{\mathrm{s1}}(\delta_1,\delta_2) \geq a_4 + a_5\cos\delta_1 - a_6 = D_{\mathrm{s1\_min}}(\delta_1) \\ D_{\mathrm{s2}}(\delta_1,\delta_2) \geq b_4 + b_5\cos\delta_2 - b_6 = D_{\mathrm{s2\_min}}(\delta_2) \end{cases} \tag{9}$$

where $D_{\mathrm{s}\,i\_\min}(\delta_i)$ is only the function of the local power angle δ_i. Therefore, the work done by $D_{\mathrm{s}\,i}$ can be scaled as follows:

$$\begin{cases} \int D_{\mathrm{s1}}(\delta_1,\delta_2)\omega_1 \mathrm{d}\delta_1 > \int D_{\mathrm{s1\_min}}(\delta_1)\omega_1 \mathrm{d}\delta_1 \\ \int D_{\mathrm{s2}}(\delta_1,\delta_2)\omega_2 \mathrm{d}\delta_2 > \int D_{\mathrm{s2\_min}}(\delta_2)\omega_2 \mathrm{d}\delta_2 \end{cases}. \tag{10}$$

The scaling process proposed earlier transforms the nonintegrable interaction terms (the red line) to the integrable terms shown in Fig. 4. Therefore, the EAC can be extended to the paralleled-converters system, as illustrated in the next section.

The multipendulum stability of the nondissipative system (4) is very complicated, metathetically [16], [23]. In practice, the power system instability and fault removal usually occur in the first pendulum process, so this article mainly focuses on the stability of the system's first pendulum, which is feasible for the nondissipative system.

IV. Stability Analysis Based on the Proposed Dual-Iteration EAC

In Section III, the nonintegrable interactive terms are scaled to integrable ones, thus laying the prerequisite for extending the EAC method to the paralleled-converters system. However, the scaling process in (5) and (6) is determined by the stable boundaries of power angles, while the boundaries are derived by the scaled terms in return. This contradiction can be neatly solved by an iterative method proposed in this section with less conservatism caused by the potential over-scaling. Meanwhile, it can be proved that the self-damping terms D_{si} have no effect on the upper stable boundary $\delta_{i\max}$. The proof is given in Appendix B. Therefore, the effect of D_{si} on system stability can be analyzed separately. A dual-iterative EAC method is proposed as follows to obtain the estimation of stable boundaries based on the scaled methods proposed in Section III, including two iteration processes:

1) *Iteration A*: The iteration for $P_{\mathrm{int}\,i}$ and $\omega_k D_{\mathrm{m}\,i}$ is conducted to obtain an estimation of the upper boundary $\delta_{i\max}$ and lay the foundation for the subsequent calculation of $\delta_{i\min}$ in (16) and (17). The stable boundaries [$\delta_{i\mathrm{minA}\_j}$, $\delta_{i\mathrm{maxA}\_j}$] obtained at each iteration are used as the input for the next iteration's inequality scaling of $P_{\mathrm{int}\,i\_\min}$ and $\omega_{k\max} D_{\mathrm{m}\,i\_\min}$ in (5)–(8), which greatly reduce the conservatism caused by the over-scaling.
2) *Iteration B*: By iterating the frequency distribution function $\omega_{i\mathrm{B}}(\delta_i)$ through (16) and (17), the work done by $\omega_{i\mathrm{B}} D_{\mathrm{s}\,i\_\min}$ can be calculated. Therefore, the effects of the self-damping terms on the stability boundaries are fully considered.

In general, the impacts of interactive electromagnetic power and mutual-damping terms are considered in Iteration A to obtain the estimation of the upper stability boundary $\delta_{i\max}$. Furthermore, the impacts of self-damping terms are considered in Iteration B to derive the estimation of lower boundary $\delta_{i\min}$, based on the results from Iteration A.

A. Process of Iteration A

To reduce conservatism caused by the potential over-scaling of $P_{\mathrm{int}\,i\_\min}$ and $\omega_{k\max} D_{\mathrm{m}\,i\_\min}$ in (5)–(8), an iterative calculation is proposed to renew the estimation of the stability boundary [$\delta_{i\mathrm{minA}\_j}$, $\delta_{i\mathrm{maxA}\_j}$] in each iteration, and regard it as the new basis for the scaling in the next iteration, as shown in Fig. 5. Define the equivalent mechanical power $P_{1\mathrm{A}\_j}$ in the jth Iteration A as follows:

$$\begin{cases} P_{1\mathrm{A}\_j} = a_0 - P_{\mathrm{int1}\_\min}(\delta_{2\mathrm{minA}\_j}) \\ -\omega_{2\mathrm{maxA}\_j} D_{\mathrm{m1}\_\min}(\delta_{2\mathrm{maxA}\_j}) \\ P_{2\mathrm{A}\_j} = b_0 - P_{\mathrm{int2}\_\min}(\delta_{1\mathrm{minA}\_j}) \\ -\omega_{1\mathrm{maxA}\_j} D_{\mathrm{m2}\_\min}(\delta_{1\mathrm{maxA}\_j}) \end{cases} \tag{11}$$

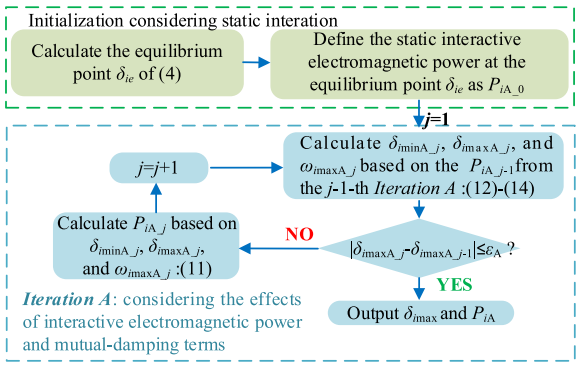

Fig. 5. Iteration flow chart for the interactive electromagnetic power and mutual-damping terms based on Iterative A.

where $\omega_{i\mathrm{maxA}\_j}$, $\delta_{i\mathrm{minA}\_j}$, and $\delta_{i\mathrm{maxA}\_j}$ denote the values for VSC$_i$ obtained in the jth Iteration A, which are derived based on EAC

$$\delta_{1\max\mathrm{A}\_j} = \pi - \sin^{-1}(P_{1\mathrm{A}\_j-1}/a_1)$$
$$\delta_{2\max\mathrm{A}\_j} = \pi - \sin^{-1}(P_{2\mathrm{A}\_j-1}/b_1) \tag{12}$$

$$\int_{\delta_{1\min\mathrm{A}\_j}}^{\delta_{1\max\mathrm{A}\_j}} [P_{1\mathrm{A}\_j-1} - a_1\sin\delta_1]\mathrm{d}\delta_1 = \int_{\delta_{2\min\mathrm{A}\_j}}^{\delta_{2\max\mathrm{A}\_j}} [P_{2\mathrm{A}\_j-1} - b_1\sin\delta_2]\mathrm{d}\delta_2 = 0 \tag{13}$$

$$\begin{cases} 0.5M_1\omega_{1\mathrm{maxA}\_j}^2 = \int_{\pi-\delta_{1\mathrm{maxA}\_j}}^{\delta_{1\mathrm{maxA}\_j}} [a_1\sin\delta_1 - P_{1\mathrm{A}\_j-1}]\mathrm{d}\delta_1 \\ 0.5M_2\omega_{2\mathrm{maxA}\_j}^2 = \int_{\pi-\delta_{2\mathrm{maxA}\_j}}^{\delta_{2\mathrm{maxA}\_j}} [b_1\sin\delta_2 - P_{2\mathrm{A}\_j-1}]\mathrm{d}\delta_2 \end{cases} \tag{14}$$

The initialization of Iteration A is derived by only considering the static interactive power: $P_{1\mathrm{A}\_0} = a_0 - a_2\sin\delta_{2\mathrm{e}} - a_3\sin(\delta_{12\mathrm{e}} + \varphi_{\mathrm{E1}})$. The condition for the end of Iteration A is that $\delta_{i\mathrm{maxA}\_j}$ converges to a given threshold ε_{A}. $\delta_{i\mathrm{maxA}}$ is output as the upper boundary estimation $\delta_{i\max}$ of VSC$_i$. $\delta_{i\mathrm{minA}\_j}$ is not output as the lower boundary estimation because it does not capture the impact of D_{si}. However, $\delta_{i\mathrm{minA}\_j}$ serves as the basis for the inequality scaling of $P_{i\mathrm{A}\_j}$ and affects the estimation of system stability boundary indirectly.

As shown in Fig. 6, the upper boundary $\delta_{1\mathrm{maxe}}$ obtained by only considering the static interaction may easily cause misjudgment since it completely ignores the adverse impacts of dynamic interactive electromagnetic power P_{int1} and varying damping. $\delta_{1\mathrm{maxc}}$ is the stability boundary obtained by the scaling method proposed in [23], which is too conservative due to the over-scaling of the interactive terms (based on the boundedness of sin and cos terms) and the positive-damping restriction (the damping $\omega_1 K_{\mathrm{p1}} V_{\mathrm{g}}\cos\delta_1$ in conventional constant impedance model in [23] should be positive: $\delta_{1\max} = \pi/2$). The upper boundary obtained by Iteration A is $\delta_{1\max}$, and the real upper boundary by simulation is $\delta_{1\mathrm{maxr}}$. Iteration A estimates the worst (maximum) equivalent mechanical power $P_{1\mathrm{A}\_j}$ (blue dashed line), by inequality scaling of the nonintegrable interactive electromagnetic power P_{int1} (green solid curve) and the mutual damping term $\omega_2 D_{\mathrm{m1}}$(blue solid curve). The proposed

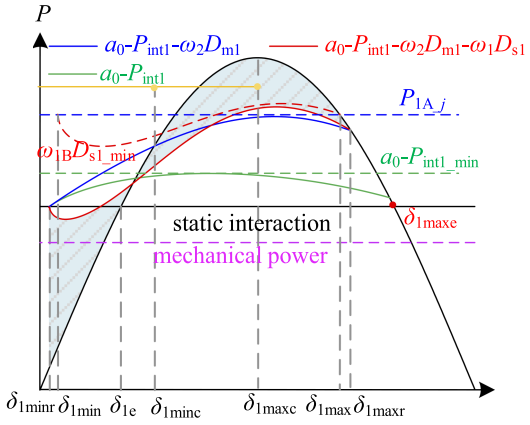

Fig. 6. Accelerating and decelerating area diagram for the paralleled converter system with the proposed DITEAC method.

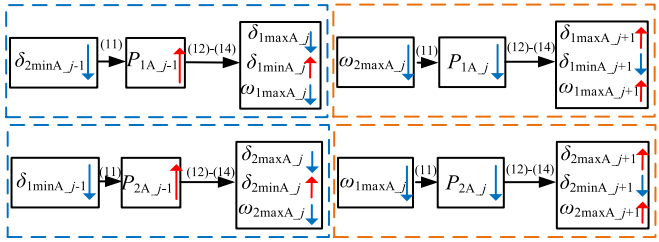

Fig. 7. Negative feedback mechanisms in Iteration A.

iterative method could greatly reduce conservatism caused by the scaling of interactive terms (compared with δ_{1maxc}), and eliminates the risk of misjudgment by considering the adverse impacts of dynamic interaction and damping terms (compared with δ_{1maxe}).

In Fig. 7, it is revealed that there exist two negative feedback mechanisms to guarantee the convergence of the designed iterative calculation. The decreasing $\delta_{2minA\_j\text{-}1}$ will lead to larger $P_{1A\_j\text{-}1}$ and smaller maximum decelerating area, and thus causes smaller ω_{1maxA_j} and larger δ_{1min_j}according to (12)–(14). Meanwhile, a smaller ω_{2maxA_j} leads to a smaller P_{1A_j}, thus resulting in a larger ω_{1maxA_j+1} in return. Similar negative feedback mechanisms exist for VSC_2. The convergence process under given system parameters is shown in Fig. 10.

B. Process of Iteration B

Based on the result from Iteration A, the impact of self-damping can be furthermore fully captured in Iteration B to estimate the lower boundary $\delta_{i\min}$. First, the equivalent mechanical power P_{iB} of Iteration B is defined as $P_{iB} = P_{iA}$, where all terms in (4) except $\omega_i D_{si}$ are considered. Applying the EAC theory to the scaled system, the frequency distribution function $\omega_{iB}(\delta_i)$ can be derived as follows:

$$\begin{cases} \dfrac{M_1\omega_{1B}^2(x)}{2} = \int_x^{\delta_{1max}} [a_1 \sin\delta_1 + \omega_{1B}(\delta_1) D_{s1\_min}(\delta_1) - P_{1B}]\,\mathrm{d}\delta_1 \\ \dfrac{M_2\omega_{2B}^2(x)}{2} = \int_x^{\delta_{2max}} [b_1 \sin\delta_2 + \omega_{2B}(\delta_2) D_{s2\_min}(\delta_2) - P_{2B}]\,\mathrm{d}\delta_2 \end{cases} \tag{15}$$

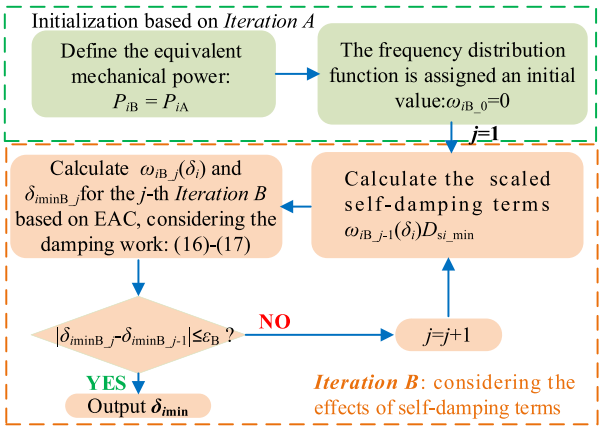

Fig. 8. Iteration flow chart for the self-damping terms based on Iteration B.

However, (15) is an implicit equation about $\omega_{iB}(\delta_i)$, which cannot be solved directly. Iteration B is thus proposed to solve (15) by iterating over frequency $\omega_{iB}(\delta_i)$ and damping work $\omega_{iB}(\delta_i)D_{si\_min}(\delta_i)$ to quantitatively estimate the effect of D_{si_min}. The iteration flow chart for Iteration B is summarized in Fig. 8.

Based on the $\omega_{iB\_j\text{-}1}(\delta_i)$ obtained from the *j*-1-th iteration, $\omega_{iB\_j}(\delta_i)$ in the *j*th iteration can be derived as follows:

$$\begin{cases} \dfrac{M_1\omega_{1B\_j}^2(x)}{2} = \int_x^{\delta_{1max}} [a_1 \sin\delta_1 \\ \quad + \omega_{1B\_j-1}(\delta_1) D_{s1\_min}(\delta_1) - P_{1B}]\,\mathrm{d}\delta_1 \\ \dfrac{M_2\omega_{2B\_j}^2(x)}{2} = \int_x^{\delta_{2max}} [b_1 \sin\delta_2 \\ \quad + \omega_{2B\_j-1}(\delta_2) D_{s2\_min}(\delta_2) - P_{2B}]\,\mathrm{d}\delta_2 \end{cases} . \tag{16}$$

The lower boundary δ_{iminB_j} in *j*th iteration is derived as follows:

$$\begin{cases} \int_{\delta_{1minB\_j}}^{\delta_{1max}} [a_1 \sin\delta_1 + \omega_{1B\_j-1}(\delta_1) D_{s1\_min}(\delta_1) - P_{1B}]\,\mathrm{d}\delta_1 = 0 \\ \int_{\delta_{2minB\_j}}^{\delta_{2max}} [b_1 \sin\delta_2 + \omega_{2B\_j-1}(\delta_2) D_{s2\_min}(\delta_2) - P_{2B}]\,\mathrm{d}\delta_2 = 0 \end{cases} . \tag{17}$$

The initial value of frequency distribution function $\omega_{iB\_0}(\delta_i)$ is derived by assuming $\omega_{iB\_0} = 0$. The condition for the end of Iteration B is that δ_{iminB_j} converges to a given threshold ε_B. δ_{iminB} is output as the lower boundary estimation $\delta_{i\min}$ of VSC_i.

Through the inequality scaling in (9) and the iteration in (16) and (17), the most adverse impacts from the self-damping term $\omega_i D_{si}$ are estimated as the red dashed line shown in Fig. 6. The real lower boundary is δ_{1minr}. The over-scaling inequality and the positive-damping restriction in [23] will result in a relatively large δ_{1minc}, that even the equilibrium point δ_{1e} may be excluded from its boundary: $\delta_{1minc} > \delta_{1e}$.

The relationship between the two iteration processes is demonstrated in Fig. 9. To sum up, $\delta_{i\max}$ is obtained by considering the interactive electromagnetic power terms and the mutual damping terms through Iteration A; based on the result from Iteration A, $\delta_{i\min}$ is obtained by considering self-damping terms through Iteration B. Therefore, the accurate stable boundary estimation of the paralleled-converters system $[\delta_{i\min}, \delta_{i\max}]$ is obtained by the proposed dual-iterative EAC method.

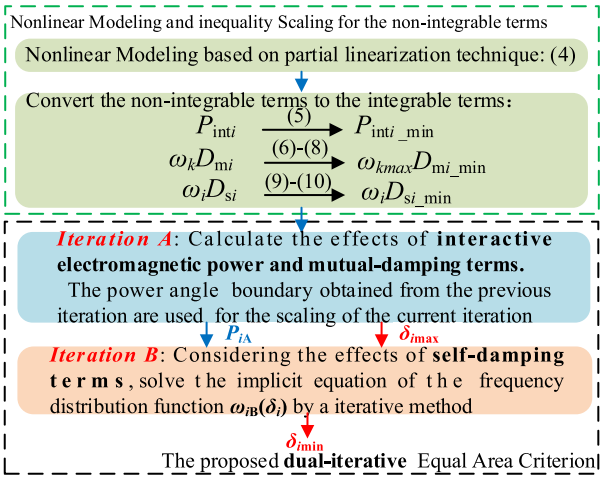

Fig. 9. Overall flow chart of the proposed dual-iterative EAC method.

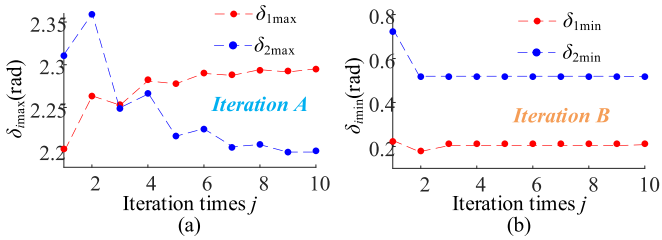

Fig. 10. Convergence process of the proposed dual-iterative EAC method.

C. Conservatism Improvement for the Iterative Algorithm

The obtained stability boundaries may be conservative, due to the scaling process of the mutual damping terms in (6)–(8). This shortcoming can somewhat be improved with a mapping function. Adopting the projection algorithm, the binary variables function: $\omega_k D_{\text{m}i}(\delta_i,\delta_k)$ can be mapped to a single variable function as follows:

$$\begin{cases} P_{\text{IDm1}\_j}(\delta_1) = \min\limits_{\delta_2 \in [\delta_{2\min A\_j}, \delta_{2\max A\_j}]} \\ \{\omega_2[a_7 + a_8\cos\delta_2 + a_9\cos(\delta_{21} + \varphi_{D12})]\} \\ P_{\text{IDm2}\_j}(\delta_2) = \min\limits_{\delta_1 \in [\delta_{1\min A\_j}, \delta_{1\max A\_j}]} \\ \{\omega_1[b_7 + b_8\cos\delta_1 + b_9\cos(\delta_{12} + \varphi_{D22})]\} \end{cases}. \quad (18)$$

Therefore, $P_{i\text{A}\_j}$ can be rewritten as follows:

$$\begin{cases} P_{1\text{A}\_j} = a_0 - P_{\text{int1}\_\min}(\delta_{2\min A\_j}) - P_{\text{IDm1}\_j}(\delta_1) \\ P_{2\text{A}\_j} = b_0 - P_{\text{int2}\_\min}(\delta_{1\min A\_j}) - P_{\text{IDm2}\_j}(\delta_2) \end{cases}. \quad (19)$$

By applying (18) and (19) in Iteration A, a more accurate stability boundary can be obtained. It should be mentioned that the high accuracy of (18) and (19) is achieved by the cost of increasing complexity in the iteration process. Therefore, whether the improvement needs to be utilized depends on whether the coefficients of mutual-damping terms are much larger than other terms. If the conservatism of the result is acceptable, it is unnecessary to use the complicated scaling in (18) and (19). Fig. 10 shows the results of the proposed dual-iterative EAC method, the accurate stability boundary can be obtained after finite (about 5–7) times iterations.

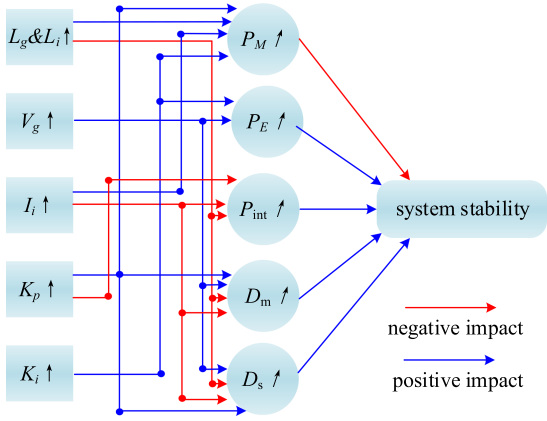

Fig. 11. Influence of system parameters on system stability.

TABLE I
IMPACT ANALYSIS OF GRID INDUCTANCE

L_g	Boundary of VSC_1(rad)	Boundary of VSC_2(rad)
1.5mH	[-1.700, 2.652]	[-1.264, 2.712]
2.0mH	[-1.086, 2.536]	[-0.636, 2.569]
3.0mH	[0.212, 2.294]	[0.517, 2.200]
3.5mH	[0.691, 2.121]	[0.782, 2.084]

TABLE II
SIMULATION PARAMETERS OF THE CONVERTER SYSTEM

Symbols	Description	Nominal value
$V_{dc1,2}$	dc-link voltage of $\text{VSC}_{1,2}$	800V
$K_{p1,2}$, $K_{i1,2}$	Controller parameters of $\text{PLL}_{1,2}$	0.5, 80
L_g	grid inductance	3mH
R_g	gird resistance	0.15 Ω
$L_{1,2}$	Line inductance of $\text{VSC}_{1,2}$	1 mH
V_g	Magnitude of microgrid voltage	220√2V
ω_n	Rated angle frequency	100πrad/s
$I_{ref1,2}$	Magnitude of reference current of $\text{VSC}_{1,2}$	150A, 50A
$\varepsilon_{\text{A,B}}$	Threshold of Iteration A/B	2×10^{-3}rad

D. Impacts of System Parameters on Transient Stability

Based on the above-mentioned analysis, the impacts of system parameters on the paralleled-converters system are revealed as shown in Fig. 11. A larger L_i or L_g will result in a larger P_{M} and smaller P_{int}, both have adverse impacts on system stability. Meanwhile, larger L_i leads to smaller damping, which is also unfavorable to stability. Table I presents estimates of stable boundaries under different inductances based on the proposed DITEAC, and other parameters are listed in Table II. It is seen that the stability boundary of the system does decrease with the increase of inductance, that is, the weaker the strength of the grid, the greater the interaction effect of the system, and the more prone to instability. Similarly, larger current reference I_i also has negative impacts on stability since it always appears together with L_i in the dynamic (4). A larger V_{g} leads to a larger P_{E} and larger damping, both benefit stability. The impacts of K_{i} & K_{p} are complicated. The increase of K_i has a positive

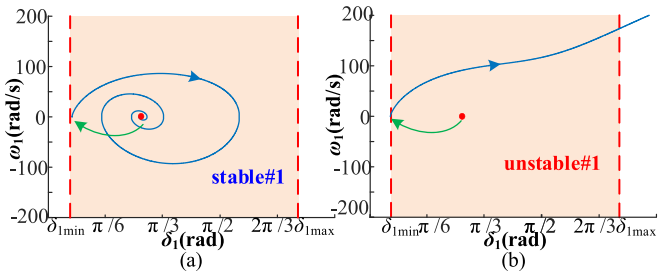

Fig. 12. Simulation verification of paralleled-converters system under different current disturbances on VSC_1. (a) Stable operation under critical disturbance. (b) Unstable operation under larger disturbance.

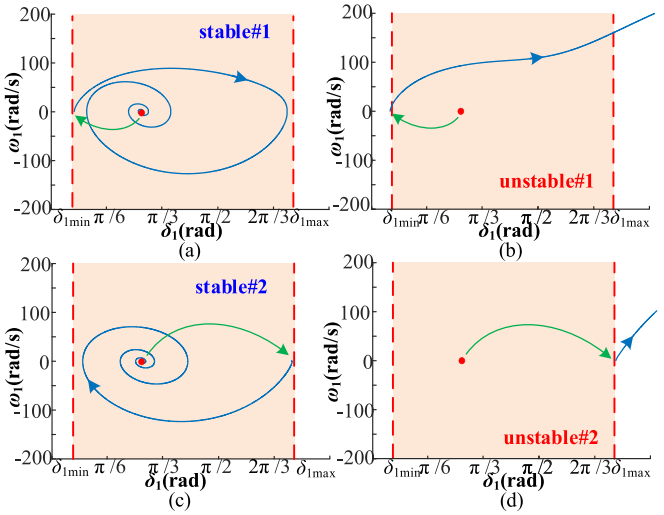

Fig. 13. Simulation verification of paralleled-converters system under different grid phase disturbances: (a) and (b) Verification of $\delta_{1\min}$. (c) and (d) Verification of $\delta_{1\max}$.

impact on P_{M} (deteriorates stability) and P_{E} (benefits stability). Meanwhile, the increasing K_{p} leads to a larger P_{M} (deteriorates stability), but also a larger damping (benefits stability). However, K_{p} cannot be too large to violate the stability condition $M_i > 0$. It should be noted that the size of the transient stability region is not the only basis for selecting parameters. Other indexes such as dynamic response should also be considered.

V. Verification

To verify the effectiveness of the proposed dual-iterative EAC method, simulations under different operation conditions are conducted with MATLAB/Simulink. Furthermore, the hardware-in-loop (HIL) experiments are carried out on the RT-Lab platform. The system parameters are listed in Table II and the stable operating points are $\delta_{\mathrm{e}1} = 0.851$ and $\delta_{\mathrm{e}2} = 0.722$ rad. The verification is executed by adding disturbances on the reference current $I_{\mathrm{ref}i}$ and the grid voltage phase θ_{g} to simulate continuous disturbances from the renewable energy side and the grid, respectively. Furthermore, a three-phase short circuit verification is given to show how the proposed method obtains the critical clearing time (CCT).

Based on the proposed dual-iterative EAC method [with the improvement in (18) and (19)], the estimation of the stable boundary of the paralleled-converters system is

$$\begin{cases} [\delta_{1\,\min}, \delta_{1\,\max}] = [0.212\,\text{rad}, 2.294\,\text{rad}] \\ [\delta_{2\,\min}, \delta_{2\,\max}] = [0.517\,\text{rad}, 2.200\,\text{rad}] \end{cases}. \tag{20}$$

The instability phenomena could be reflected by the escaping phase trajectory from the stable boundary. Therefore, the phase trajectory is characterized when verifying the proposed method.

A. Simulation Verification

1) Under the Grid Current Disturbance: Simulation results under different current disturbances are given in Fig. 12. As shown in Fig. 12(a), after the system encounters a critical disturbance in VSC_1 from $I_{\mathrm{sta}} = 16$ A ($\delta_1(t_0) = 0.2168$ rad $> \delta_{1\min}$) to I_{ref1}, the phase trajectories are always inside the stable boundary during the oscillation process, the system remains stable and returns to equilibrium. However, when the system encounters a larger disturbance in VSC_1 from $I_{\mathrm{uns}} = 8$ A ($\delta_1(t_0) = 0.1857$ rad $< \delta_{1\min}$) to I_{ref1}, the power angle δ_1 exceeds its minimum stability boundary, which eventually leads to instability as in Fig. 12(b). The simulation results are highly consistent with the theoretical analysis.

2) Under the Grid Phase Disturbance: The simulation verification of $\delta_{1\min}$ is carried out in Fig. 13(a) and (b), where the system encounters the critical grid phase disturbance: stable#1 ($\delta_{1\mathrm{sta}\#1\min} = 0.2135$ rad) and larger disturbance: unstable#1 ($\delta_{1\mathrm{uns}\#1\min} = 0.1735$ rad), respectively. The power angle δ_1 of VSC_1 shows different stability characteristics but is consistent with the theoretical analysis. Similar verification of $\delta_{1\max}$ is given in Fig. 13(c) and (d). After the system encounters a critical stable disturbance ($\delta_{1\mathrm{sta}\#2\max} = 2.2663$ rad) and a larger disturbance ($\delta_{1\mathrm{uns}\#2\max} = 2.3063$ rad), the system remains stable and loses stability, respectively. The simulation results show high consistency with the analysis earlier and therefore verify the effectiveness of the proposed method in the estimation of VSC_1's stable boundary.

Similar verification can be carried out for the obtained stable boundary of VSC_2. In Fig. 14(a) and (c), the system encounters critical stable grid phase disturbance: $\delta_{2\mathrm{sta}\#1\min} = 0.520$ rad and $\delta_{2\mathrm{sta}\#2\max} = 2.1246$ rad. The system remains stable after both disturbances and returns to equilibrium since they are within the stable boundary. The larger conservatism of $\delta_{2\min}$ is because that the larger I_1 leads to the larger self-damping interaction term b_6 (approximately 3 times that of a_6). Therefore, the proposed mathematical scaling on a_6 inevitably brings conservatism. However, the correctness of the proposed method is not violated since it does not misjudge the unstable transient process as stable. Conservatism is an unavoidable defect of almost all transient stability analysis methods, but the proposed iterative method greatly reduces conservatism compared with existing analysis methods [23]. When the system encounters larger disturbance: $\delta_{2\mathrm{uns}\#1\min} = 0.0718$ rad and $\delta_{2\mathrm{uns}\#2\max} = 2.3246$ rad, the trajectory crosses the boundary and loses stability as shown in Fig. 14(b) and (d). The system shown in Fig. 14(b) is unstable because the trajectory of VSC_2's trajectory

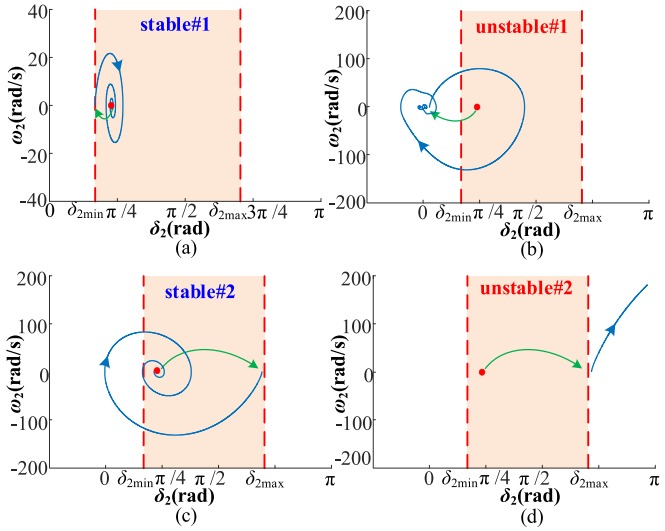

Fig. 14. Simulation verification of paralleled-converters system under different grid phase disturbances. (a) and (b) Verification of $\delta_{2\min}$. (c) and (d) Verification of $\delta_{2\max}$.

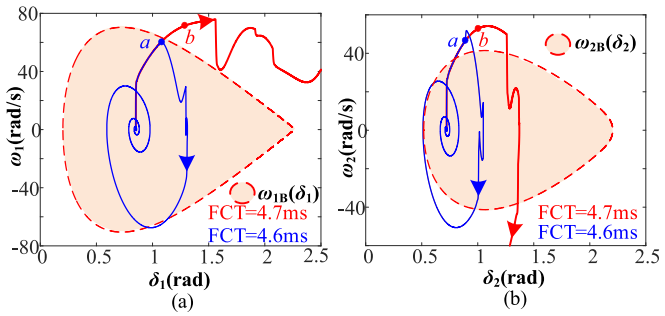

Fig. 15. Simulation verification of paralleled-converters system under three-phase short-circuit fault with clearing. (a) VSC_1. (b) VSC_2.

does not return to equilibrium but moves chaotically outside the stable boundary. This is because the instability of VSC_1 leads to the failure of VSC_2 to operate at the normal stable operating point, so the whole system is also regarded as unstable. Based on the above-mentioned simulation results, the accuracies of $\delta_{2\min}$ and $\delta_{2\max}$ are fully verified, since they are in accord with the theoretical analysis.

3) Under Three-Phase Short-Circuit Fault With Clearing: To further verify the effectiveness and accuracy of the proposed DITEAC, the simulation verification under three-phase short-circuit fault with fault clearing is shown in Fig. 15. The short circuit inductance is $L_S = 3$ mH. The short circuit occurs at the midpoint between the grid and the parallel point of VSCs. The frequency distribution function $\omega_{i\mathrm{B}}(\delta_i)$ is the critical stable trajectory estimation of the system after scaling. Therefore, when the system is still within $\omega_{i\mathrm{B}}(\delta_i)$ after fault removal, the system can remain stable; otherwise, stability cannot be guaranteed. As shown in Fig. 15(a), when the fault is cleared (at point a) within the frequency disturbance function $\omega_{1\mathrm{B}}(\delta_1)$, where the fault clearing time (FCT) is 4.6 ms, the system remains stable and

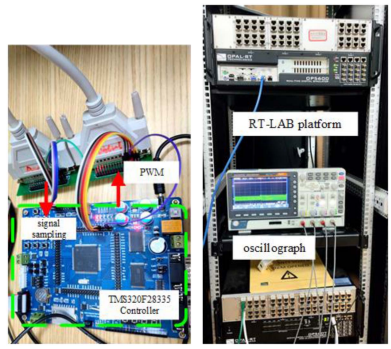

Fig. 16. HIL experimental test rig with RT-Lab platform.

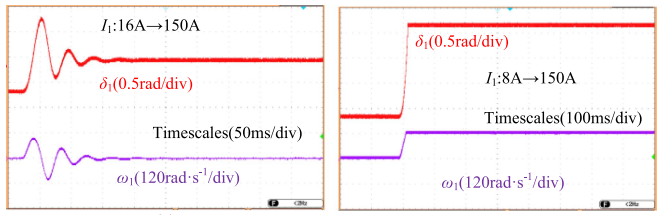

Fig. 17. Experimental verification of VSC_1 under current reference disturbances. (a) Stable within the boundary. (b) Unstable out the boundary.

returns to equilibrium after the transient process. The system will lose stability if the fault is cleared (at point b) outside $\omega_{1\mathrm{B}}(\delta_1)$, where the FCT is 4.7 ms. In contrast, the stability boundary of VSC_2 is slightly more conservative. As shown in Fig. 15(b) point a is already outside $\omega_{2\mathrm{B}}(\delta_2)$ but the system is still stable. Conservatism is unavoidable, but VSC_1 is still within the stable boundary when the fault is cleared at point a, so the system is still considered to be stable.

B. HIL Experimental Verification

To fully validate the effectiveness of the proposed DITEAC, a HIL test rig is built based on the RT-LAB platform, and the control algorithm is implemented in DSP28335, shown in Fig. 16.

1) Under Grid Current Disturbances: After the system encounters a critical disturbance in VSC_1 from the initial value: $I_{\mathrm{sta}} = 16$ A to I_{ref1}, the initial value of δ_1 before the disturbance $\delta_1(t_0) = 0.2168$ rad is still within the stable boundary. Therefore, the system should remain stable after the disturbance based on the above-mentioned analysis, which is consistent with the experimental response shown in Fig. 17(a). When a larger disturbance $I_{\mathrm{uns}} = 8$ A is applied to VSC_1's current reference, the initial power angle $\delta_1(t_0) = 0.1857$ rad, exceeds the lower stable boundary of δ_1. Therefore, the system will lose stability according to the proposed method. The experimental results show high consistency with the theoretical analysis and lose stability as shown in Fig. 17(b).

2) Under Grid Phase Disturbance: The disturbances of δ_1 are set as -0.639 and -0.667 rad on its nominal value, to verify

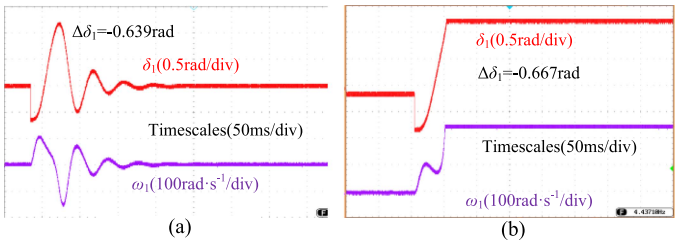

Fig. 18. Experimental verification of $\delta_{1\min}$ under grid phase disturbances. (a) Stable within the boundary. (b) Unstable out the boundary.

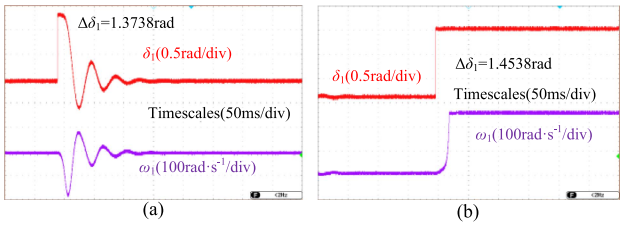

Fig. 19. Experimental verification of $\delta_{1\max}$ under grid phase disturbances. (a) Stable within the boundary. (b) Unstable out the boundary.

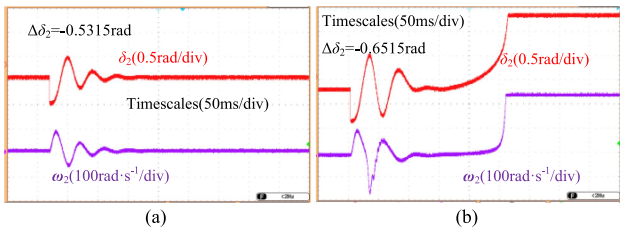

Fig. 20. Experimental verification of $\delta_{2\min}$ under grid phase disturbances. (a) Stable within the boundary. (b) Unstable out the boundary.

the accuracy and validity of $\delta_{1\min}$. As shown in Fig. 18(a), the system remains stable when the disturbance is within the critical value. As shown in Fig. 18(b), the system becomes unstable when the disturbance exceeds the critical value. Fig. 19 shows the experimental verification of $\delta_{1\max}$. When the grid phase disturbance $\Delta\delta_1 = 1.3738$ is within the upper boundary, the system remains stable as shown in Fig. 19(a). The system loses stability when the applied disturbance $\Delta\delta_1 = 1.4538$ exceeds the upper boundary, as shown in Fig. 19(b).

Similar verification is carried out to validate the accuracy of VSC_2's stable boundary. Fig. 20(a) and (b) show the experimental responses when the grid phase disturbance is $\Delta\delta_2 = -0.5315$ rad and -0.6515 rad, respectively. As shown in Fig. 21(a), the system remains stable when $\Delta\delta_2 = 1.4063$ rad is within the upper boundary $\delta_{2\max}$ of VSC_2. Instability phenomena occur when $\Delta\delta_2 = 1.6063$ rad exceeds $\delta_{2\max}$, as shown in Fig. 21(b). The experimental responses of the validation of VSC_2's stable boundary are consistent with the theory proposed in this article.

3) Under Three-Phase Short-Circuit Fault With Clearing: The RT-Lab experimental verification for paralleled converters under three-phase short-circuit fault with different clearing times

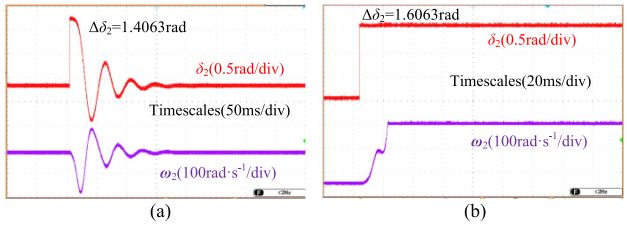

Fig. 21. Experimental verification of $\delta_{2\max}$ under grid phase disturbances. (a) Stable within the boundary. (b) Unstable out the boundary.

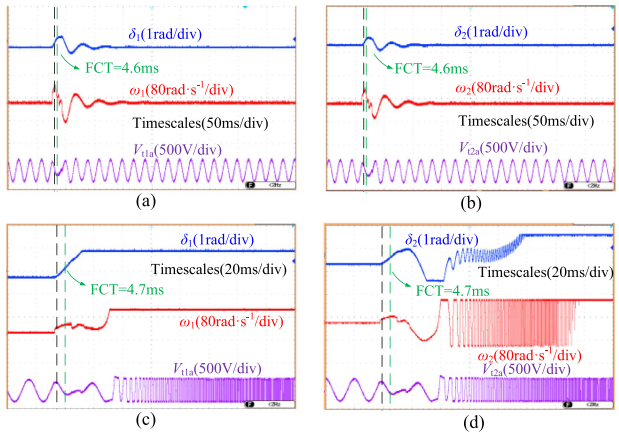

Fig. 22. Experimental verification for paralleled converters under three-phase short-circuit fault. (a) and (b) Stable operation (FCT = CCT = 4.6 ms). (c) and (d) Unstable operation (FCT = 4.7 ms > CCT = 4.6 ms).

TABLE III
COMPARISON OF DIFFERENT METHODS

Method	Boundary of VSC_1(rad)	Boundary of VSC_2(rad)
DITEAC	[0.212, 2.294]	[0.517, 2.200]
$CEAC_1$ (ignore damping)	[0.170, 2.282]	[-0.213, 2.426]
$CEAC_2$ (consider damping)	[0.606, 1.571]	[0.720, 1.571]
Simulation results	[0.174, 2.300]	[0.073, 2.324]

are shown in Fig. 22. The parameters are consistent with the simulation in Fig. 15. As shown in Fig. 22(a) and (b), when the grid fault is removed before the CCT (FCT = CCT = 4.6 ms), the system could remain stability. However, as shown in Fig. 22(c) and (d), when the grid fault is removed after the CCT (FCT = 4.7 ms > CCT = 4.6 ms), the system loses stability. The experimental responses of the validation of three-phase short circuit are consistent with the proposed DITEAC.

C. Comparison of Different Methods

With the system parameters given in Table II, the simulation results and the estimation of the system stable boundary based on the $CEAC_1$ ignoring the varying damping [23], the $CEAC_2$ considering the varying damping, and the proposed DITEAC are compared in Table III. Due to the ignorance of the adverse impacts caused by the negative damping and the imprecise modeling, the $CEAC_1$'s results are larger than the real boundary by simulation, which may misjudge an unstable

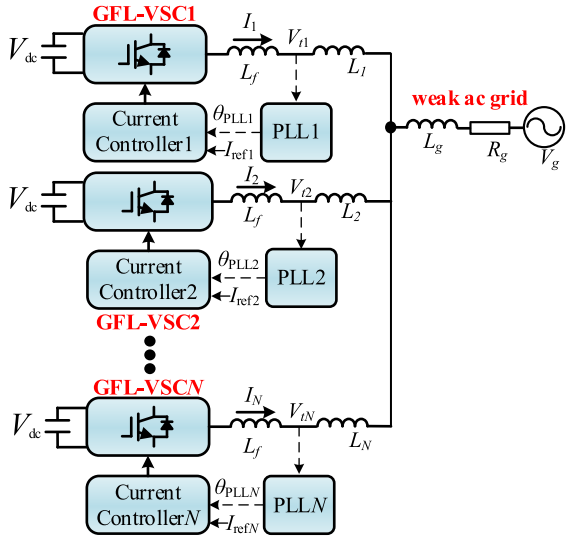

Fig. 23. Topology and control strategy of the *N*-converters system.

system to be stable. This kind of misjudgment is unacceptable for practical application [16], whereas the conservatism of criteria is acceptable. However, due to the large conservatism caused by the over-scaling in interaction and the positive-damping restriction, the stable boundary obtained by CEAC_2 is too conservative, which may cause the malfunction of protection systems for practical application. In contrast, DITEAC not only adopts a more accurate model but also fully captures the impacts of damping on stability. In addition, DITEAC uses a combination of mathematical scaling and iteration, which greatly improves the conservatism of the existing method and shows a strong superiority in engineering applications.

VI. Discussion of Modeling and Stability Analysis of Multi-VSCs System

The main contents of this article are based on the dual-converters system as shown in Fig. 1. This section extends the modeling to the *N*-converters system, and discusses the scalability of the proposed dual-iterative EAC method in the *N*-converters system. Consider an *N*-converters system shown in Fig. 23. The corresponding network and controller parameters are consistent with the abovementioned, where the lower corner i represents the corresponding value of VSC_i.

The voltage at PCC_i can be denoted as follows:

$$\begin{aligned} V_{\text{t}i}\angle\theta_{\text{t}i} = {} & V_g\angle\theta_g + I_i(R_g + R_i)\angle(\theta_{\text{PLL}i} \\ & + \varphi_i) + R_g\sum_{k\neq i} I_k\angle(\theta_{\text{PLL}k} + \varphi_k) \\ & + (L_g + L_i)\frac{dI_i\angle(\theta_{\text{PLL}i} + \varphi_i)}{dt} \\ & + L_g\sum_{k\neq i}\frac{dI_k\angle(\theta_{\text{PLL}k} + \varphi_k)}{dt}. \end{aligned} \tag{21}$$

Applying Park translation on (21), the q-axis component of V_{ti} can be derived by assuming $\varphi_i = 0$

$$\begin{aligned} V_{tiq} = {} & V_g\sin(-\delta_i) + R_g\sum_{k\neq i} I_k\sin(\delta_{ki}) \\ & + \omega_{\text{PLL}i}I_i(L_g + L_i) + L_g\sum_{k\neq i} I_k\omega_{\text{PLL}k}\cos(\delta_{ki}). \end{aligned} \tag{22}$$

Substituting the above-mentioned equation into the dynamic equation of the PLL shown in (3), after the derivation and simplification shown in Appendix A, the state space equation can be obtained as follows:

$$\begin{aligned} M_i\ddot{\delta}_i = {} & a_0 - \sum_{k=1}^{N} a_k\sin(\delta_k) - \sum_{k=1,k\neq i}^{N} a_{ik}\sin(\delta_{ik}) \\ & - \sum_{k=1}^{N}\{[a_{D0k} + a_{D1k}\cos(\delta_k) \\ & + \sum_{m\neq k}^{N} a_{Dmk}\cos(\delta_{km} + \varphi_{Dmk})]\omega_k\}. \end{aligned} \tag{23}$$

Limited by space, the specific coefficient expression of (23) is not expanded here. However, the structure of the state space (23) of the *N*-converters system is the same as that of the dual-converters system (4). Equation (23) can also be divided into equivalent mechanical power, equivalent interactive electromagnetic power, self-damping, and mutual-damping terms. Therefore, the dual-iterative method proposed in this article can be extended to the *N*-converters system, which is also one of the primary contents of our future work. Besides, the state space equation of a single converter system also satisfies (23), by assuming $N = 1$.

VII. Conclusion

This article investigates the transient stability of a paralleled-converters system, considering the nonlinear dynamic interactions between paralleled GFL-VSCs and their interactions with the weak grid. To deal with the interactive power and the nonlinear damping terms, a DITEAC is proposed to derive the transient stability conditions. First, a novel and unified nonlinear model of the paralleled-converters system is built with the partial linearization technique, preserves the body characteristics of the system, and is applicable for transient stability analysis and nonlinear controller optimization. To convert the nonintegrable interactive terms to the integrable terms, an inequality scaling process is proposed. Compared with the conventional EAC method proposed in [23] and the static analysis methods, both the estimation accuracy and conservatism of the stability region obtained by the proposed DITEAC are greatly improved. The novelty of this article is summarized as follows:

1) The interaction between the grid and the converters is fully captured by using a variable impedance model. The unified model is further extended to the N-converters systems, and the physical meaning of each term is fully elaborated.

2) An EAC method based on the combination of mathematical scaling and iteration is proposed to fill the gap in the accurate transient stability estimation of paralleled-converter systems. The impacts of the dynamic interactive terms and the nonlinear damping terms on stability are considered skillfully and completely.
3) The proposed dual-interactive EAC method is easily extended to the *N*-converters systems. Demonstrate excellent and novel extensibility compared with the existing methods.

APPENDIX

A. Derivation of (4)

Combining (2) and (3), the dynamic of PLLs can be referred to as follows:

$$\begin{aligned}\delta''_1 &= K_{p1}V'_{PCCq1} + K_{i1}V_{PCCq1}\\ &= -K_{p1}V_g\omega_1\cos(\delta_1) + K_{p1}I_2R_g\cos(\delta_{21})(\omega_2-\omega_1)\\ &\quad + \delta''_1K_{p1}I_1(L_g+L_1) + \boldsymbol{\delta''_2K_{p1}I_2L_g\cos(\delta_{21})}\\ &\quad - \boldsymbol{K_{p1}(\delta'_2+\omega_g)I_2L_g\sin(\delta_{21})(\omega_2-\omega_1)} - K_{i1}V_g\sin(\delta_1)\\ &\quad + K_{i1}I_2R_g\sin(\delta_{21}) + K_{i1}I_1(L_g+L_1)(\omega_1+\omega_g)\\ &\quad + K_{i1}I_2L_g\cos(\delta_{21})(\omega_2+\omega_g) \qquad \text{(A1)}\\ \delta''_2 &= K_{p2}V'_{PCCq2} + K_{i2}V_{PCCq2}\\ &= -K_{p2}V_g\omega_2\cos(\delta_2) + K_{p2}I_1R_g\cos(\delta_{12})(\omega_1-\omega_2)\\ &\quad + \delta''_2K_{p2}I_2(L_g+L_2) + \boldsymbol{\delta''_1K_{p2}I_1L_g\cos(\delta_{12})}\\ &\quad - \boldsymbol{K_{p2}(\delta'_1+\omega_g)I_1L_g\sin(\delta_{12})(\omega_1-\omega_2)} - K_{i2}V_g\sin(\delta_2)\\ &\quad + K_{i2}I_1R_g\sin(\delta_{12}) + K_{i2}I_2(L_g+L_2)(\omega_2+\omega_g)\\ &\quad + K_{i2}I_1L_g\cos(\delta_{12})(\omega_1+\omega_g). \qquad \text{(A2)}\end{aligned}$$

The terms in bold are derived from the derivative of $(\omega_g + \omega_k)I_kL_g\cos\delta_{ki}$ in $V_{PCCq}{}_i$. They will produce the quadratic nonlinear terms: $\omega_1\omega_2$, ${\omega_1}^2$, ${\omega_2}^2$ and the coupling term $\cos(m\delta_1 - n\delta_2)$ and $\cos(m\delta_2 - n\delta_1)$, which greatly increase the difficulty of modeling and stability analysis but has little influence on the accuracy of dynamic response, which is illustrated by the time domain response in Fig. 2. Partial linearization technique is widely used to analyze the control and transient stability of chaotic systems to reduce the difficulty of analysis and increase the applicability of the stability analysis methods [24]. Apply the partial linearization technique to eliminate the above-mentioned annoying terms as follows:

$$\begin{aligned}&K_{p1}[(\omega_g+\delta'_2)I_2L_g\cos(\delta_{21})]'\\ &\approx -\omega_gK_{p1}I_2L_g\sin(\delta_{21})(\delta'_2-\delta'_1)\\ &\quad +\delta''_2K_{p1}I_2L_g\cos(\delta_{21e}) \qquad \text{(A3)}\\ &K_{p2}[(\omega_g+\delta'_1)I_1L_g\cos(\delta_{12})]'\\ &\approx -\omega_gK_{p2}I_1L_g\sin(\delta_{12})(\delta'_1-\delta'_2)\\ &\quad +\delta''_1K_{p2}I_1L_g\cos(\delta_{12e}). \qquad \text{(A4)}\end{aligned}$$

Substitute (A3) and (A4) into (A1) and (A2) and move the δ''_i term to the left side of the equation:

$$\begin{aligned}J_1\delta''_1 &= -K_{p1}V_g\omega_1\cos(\delta_1) + K_{p1}I_2R_g\cos(\delta_{21})(\omega_2-\omega_1)\\ &\quad + \delta''_2K_{p1}I_2L_g\cos(\delta_{21e}) - K_{p1}\omega_gI_2L_g\sin(\delta_{21})(\omega_2-\omega_1)\\ &\quad - K_{i1}V_g\sin(\delta_1) + K_{i1}I_2R_g\sin(\delta_{21})\\ &\quad + K_{i1}I_1(L_g+L_1)(\omega_1+\omega_g) + K_{i1}I_2L_g\cos(\delta_{21})(\omega_2+\omega_g) \qquad \text{(A5)}\\ J_2\delta''_2 &= -K_{p2}V_g\omega_2\cos(\delta_2) + K_{p2}I_1R_g\cos(\delta_{12})(\omega_1-\omega_2)\\ &\quad + \delta''_1K_{p2}I_1L_g\cos(\delta_{12e}) - K_{p2}\omega_gI_1L_g\sin(\delta_{12})(\omega_1-\omega_2)\\ &\quad - K_{i2}V_g\sin(\delta_2) + K_{i2}I_1R_g\sin(\delta_{12})\\ &\quad + K_{i2}I_2(L_g+L_2)(\omega_2+\omega_g) + K_{i2}I_1L_g\cos(\delta_{12})(\omega_1+\omega_g) \qquad \text{(A6)}\end{aligned}$$

where J_i is denoted as follows:

$$\begin{aligned}J_1 &= [1 - K_{p1}I_1(L_g+L_1)]\\ J_2 &= [1 - K_{p2}I_2(L_g+L_2)]. \qquad \text{(A7)}\end{aligned}$$

Substituting (A6) into the δ''_2 term in (A5) can obtain

$$\begin{aligned}J_1\delta''_1 &= -K_{p1}V_g\omega_1\cos(\delta_1) + K_{p1}I_2R_g\cos(\delta_{21})(\omega_2-\omega_1)\\ &\quad - K_{p1}\omega_gI_2L_g\sin(\delta_{21})(\omega_2-\omega_1) - K_{i1}V_g\sin(\delta_1)\\ &\quad + K_{i1}I_1(L_g+L_1)(\omega_1+\omega_g) + K_{i1}I_2L_g\cos(\delta_{21})(\omega_2+\omega_g)\\ &\quad + K_{i1}I_2R_g\sin(\delta_{21}) + \frac{K_{p1}I_2L_g\cos(\delta_{21e})}{J_2}\{-K_{p2}V_g\omega_2\cos(\delta_2)\\ &\quad + K_{p2}I_1R_g\cos(\delta_{12})(\omega_1-\omega_2) + \delta''_1K_{p2}I_1L_g\cos(\delta_{12e})\\ &\quad - K_{p2}\omega_gI_1L_g\sin(\delta_{12})(\omega_1-\omega_2) - K_{i2}V_g\sin(\delta_2)\\ &\quad + K_{i2}I_1R_g\sin(\delta_{12}) + K_{i2}I_2(L_g+L_2)(\omega_2+\omega_g)\\ &\quad + K_{i2}I_1L_g\cos(\delta_{12})(\omega_1+\omega_g)\}. \qquad \text{(A8)}\end{aligned}$$

Move the δ''_1 term to the left side of (A8)

$$\begin{aligned}M_1\delta''_1 &= -K_{p1}V_g\omega_1\cos(\delta_1) + K_{p1}I_2R_g\cos(\delta_{21})(\omega_2-\omega_1)\\ &\quad - K_{p1}\omega_gI_2L_g\sin(\delta_{21})(\omega_2-\omega_1) - K_{i1}V_g\sin(\delta_1)\\ &\quad + K_{i1}I_1(L_g+L_1)(\omega_1+\omega_g) + K_{i1}I_2L_g\cos(\delta_{21})(\omega_2+\omega_g)\\ &\quad + K_{i1}I_2R_g\sin(\delta_{21}) + \frac{K_{p1}I_2L_g\cos(\delta_{21e})}{J_2}\{-K_{p2}V_g\omega_2\cos(\delta_2)\\ &\quad + K_{p2}I_1R_g\cos(\delta_{12})(\omega_1-\omega_2) - K_{i2}V_g\sin(\delta_2)\\ &\quad - K_{p2}\omega_gI_1L_g\sin(\delta_{12})(\omega_1-\omega_2) + K_{i2}I_1R_g\sin(\delta_{12})\\ &\quad + K_{i2}I_2(L_g+L_2)(\omega_2+\omega_g) + K_{i2}I_1L_g\cos(\delta_{12})(\omega_1+\omega_g)\} \qquad \text{(A9)}\end{aligned}$$

where M_i denotes the virtual inertia of VSC$_i$

$$\begin{aligned}M_1 &= J_1 - \frac{1}{J_2}K_{p2}K_{p1}I_1I_2L_g^2\cos^2(\delta_{21e})\\ M_2 &= J_2 - \frac{1}{J_1}K_{p2}K_{p1}I_1I_2L_g^2\cos^2(\delta_{12e}). \qquad \text{(A10)}\end{aligned}$$

Further simplification of (A9) yields (4), where detailed expressions of coefficients are as follows:

$$
\begin{aligned}
a_0 &= \omega_g K_{i1} I_1 (L_g + L_1) + \frac{K_{p1} I_2 L_g}{J_2} \omega_g K_{i2} I_2 (L_g \\
&\quad + L_2) \cos(\delta_{21e}) \\
a_1 &= K_{i1} V_g \\
a_2 &= \frac{K_{p1} I_2 L_g}{J_2} K_{i2} V_g \cos(\delta_{21e}) \\
a_{3\sin} &= K_{i1} I_2 R_g - \frac{K_{p1} I_2 L_g}{J_2} K_{i2} I_1 R_g \cos(\delta_{21e}) \\
a_{3\cos} &= -\omega_g K_{i1} I_2 L_g - \frac{K_{p1} I_2 L_g}{J_2} \omega_g K_{i2} I_1 L_g \cos(\delta_{21e}) \\
a_3 &= \sqrt{a_{3\sin}^2 + a_{3\cos}^2} \\
\varphi_{E1} &= \arctan(a_{3\cos}/a_{3\sin}) \\
a_4 &= -K_{i1} I_1 (L_g + L_1) \\
a_5 &= K_{p1} V_g \\
a_{6\sin} &= \omega_g K_{p1} I_2 L_g + \frac{K_{p1} I_2 L_g}{J_2} \omega_g K_{p2} I_1 L_g \cos(\delta_{21e}) \\
a_{6\cos} &= \frac{-K_{p1} I_2 L_g}{J_2} K_{p2} I_1 R_g \cos(\delta_{21e}) + K_{p1} I_2 R_g \\
&\quad - \frac{K_{p1} I_2 L_g}{J_2} K_{i2} I_1 L_g \cos(\delta_{21e})
\end{aligned} \tag{A11}
$$

$$
\begin{aligned}
a_6 &= \sqrt{a_{6\sin}^2 + a_{6\cos}^2} \\
\varphi_{D11} &= -\arctan(a_{6\sin}/a_{6\cos}) \\
a_7 &= -\frac{K_{p1} I_2 L_g}{J_2} K_{i2} I_2 (L_g + L_2) \cos(\delta_{21e}) \\
a_8 &= \frac{K_{p1} I_2 L_g}{J_2} K_{p2} V_g \cos(\delta_{21e}) \\
a_{9\sin} &= \omega_g K_{p1} I_2 L_g + \frac{K_{p1} I_2 L_g}{J_2} \omega_g K_{p2} I_1 L_g \cos(\delta_{21e}) \\
a_{9\cos} &= -K_{i1} I_2 L_g + \frac{K_{p1} I_2 L_g}{J_2} K_{p2} I_1 R_g \cos(\delta_{21e}) \\
&\quad - K_{p1} I_2 R_g \\
a_9 &= -\sqrt{a_{9\sin}^2 + a_{9\cos}^2} \\
\varphi_{D12} &= \pi - \arctan(a_{9\sin}/a_{9\cos}).
\end{aligned}
$$

For VSC_2, similar derivations can be achieved by substituting (A5) into the δ''_1 term in (A6), which is not repeated here.

B. Impact Analysis of Self-Damping Terms on the Upper Boundary δ_{imax}

The necessary and sufficient condition for system stability is that the acceleration of the system should be negative when δ_i reaches the farthest right point. The self-damping terms thus have no effect on the system dynamics, since the local frequency ω_i is zero at the farthest right point δ_i. Consequently, the upper stable boundary δ_{imax} is not affected by the self-damping terms. Therefore, the effects of self-damping can be considered separately in Iteration B. In contrast, when δ_i moves to the farthest right point, there is no guarantee that ω_k is zero. Therefore, the mutual-damping terms affect the upper boundary δ_{imax} and should be considered together with the interactive electromagnetic power terms in Iteration A.

REFERENCES

[1] M. Farrokhabadi et al., "Microgrid stability definitions, analysis, and examples," *IEEE Trans. Power Syst.*, vol. 35, no. 1, pp. 13–29, Jan. 2020.

[2] Q. Zhou, Z. Tian, M. Shahidehpour, X. Liu, A. Alabdulwahab, and A. Abusorrah, "Optimal consensus-based distributed control strategy for coordinated operation of networked microgrids," *IEEE Trans. Power Syst.*, vol. 35, no. 3, pp. 2452–2462, May 2020.

[3] I. Subotić, D. Groß, M. Colombino, and F. Dörfler, "A Lyapunov framework for nested dynamical systems on multiple time scales with application to converter-based power systems," *IEEE Trans. Autom. Control*, vol. 66, no. 12, pp. 5909–5924, Dec. 2021.

[4] S. Samanta and N. R. Chaudhuri, "On stability analysis of power grids with synchronous generators and grid-forming converters under DC-side current limitation," in *Proc. Amer. Control Conf.*, 2021, pp. 1817–1823.

[5] Y. Liao and X. Wang, "Controller design-oriented analysis of grid-forming converters for stability robustness enhancement," *Chin. J. Elect. Eng.*, vol. 7, no. 4, pp. 37–48, Dec. 2021.

[6] W. Du et al., "Modeling of grid-forming and grid-following inverters for dynamic simulation of large-scale distribution systems," *IEEE Trans. Power Del.*, vol. 36, no. 4, pp. 2035–2045, Aug. 2021.

[7] M. G. Taul, X. Wang, P. Davari, and F. Blaabjerg, "An overview of assessment methods for synchronization stability of grid-connected converters under severe symmetrical grid faults," *IEEE Trans. Power Electron.*, vol. 34, no. 10, pp. 9655–9670, Oct. 2019.

[8] Y. Li, Y. Tang, Y. Lu, F. Hua, and Z. Du, "Synchronization stability of grid-connected VSC with limits of PLL," *IEEE Trans. Power Syst.*, to be published, doi: 10.1109/TPWRS.2022.3208244.

[9] M. Cespedes and J. Sun, "Impedance modeling and analysis of grid-connected voltage-source converters," *IEEE Trans. Power Electron.*, vol. 29, no. 3, pp. 1254–1261, Mar. 2014, doi: 10.1109/TPEL.2013.2262473.

[10] D. K. Dheer, A. S. Vijay, O. V. Kulkarni, and S. Doolla, "Improvement of stability margin of droop-based islanded microgrids by cascading of lead compensators," *IEEE Trans. Ind. Appl.*, vol. 55, no. 3, pp. 3241–3251, May/Jun. 2019.

[11] A. Kunwar, F. Shahnia, and R. C. Bansal, "Eigenvalue-oriented dynamic stability examination to enhance designing a microgrid hosting clusters of inertial and non-inertial distributed generators," *IEEE Trans. Smart Grid*, vol. 11, no. 3, pp. 1942–1955, May 2020.

[12] Y. Zhang, L. Xie, and Q. Ding, "Interactive control of coupled microgrids for guaranteed system-wide small signal stability," *IEEE Trans. Smart Grid*, vol. 7, no. 2, pp. 1088–1096, Mar. 2016.

[13] Q. Hu, L. Fu, F. Ma, and F. Ji, "Large signal synchronizing instability of PLL-based VSC connected to weak AC grid," *IEEE Trans. Power Syst.*, vol. 34, no. 4, pp. 3220–3229, Jul. 2019.

[14] Z. Tian et al., "Hamilton-based stability criterion and attraction region estimation for grid-tied inverters under large-signal disturbances," *IEEE J. Emerg. Sel. Topics Power Electron.*, vol. 10, no. 1, pp. 413–423, Feb. 2022.

[15] X. Fu et al., "Large-signal stability of grid-forming and grid-following controls in voltage source converter: A comparative study," *IEEE Trans. Power Electron.*, vol. 36, no. 7, pp. 7832–7840, Jul. 2021.

[16] Y. Tang, Z. Tian, X. Zha, X. Li, M. Huang, and J. Sun, "An improved equal area criterion for transient stability analysis of converter-based microgrid considering nonlinear damping effect," *IEEE Trans. Power Electron.*, vol. 37, no. 9, pp. 11272–11284, Sep. 2022.

[17] H. Wu and X. Wang, "Design-oriented transient stability analysis of PLL-synchronized voltage-source converters," *IEEE Trans. Power Electron.*, vol. 35, no. 4, pp. 3573–3589, Apr. 2020.

[18] J. Zhao, M. Huang, H. Yan, C. K. Tse, and X. Zha, "Nonlinear and transient stability analysis of phase-locked loops in grid-connected converters," *IEEE Trans. Power Electron.*, vol. 36, no. 1, pp. 1018–1029, Jan. 2021.

[19] Y. Zhang, C. Zhang, and X. Cai, "Large-signal grid-synchronization stability analysis of PLL-based VSCs using Lyapunov's direct method," *IEEE Trans. Power Syst.*, vol. 37, no. 1, pp. 788–791, Jan. 2022.
[20] C. Shen et al., "Transient stability and current injection design of paralleled current-controlled VSCs and virtual synchronous generators," *IEEE Trans. Smart Grid*, vol. 12, no. 2, pp. 1118–1134, Mar. 2021.
[21] X. He and H. Geng, "PLL synchronization stability of grid-connected multiconverter systems," *IEEE Trans. Ind. Appl.*, vol. 58, no. 1, pp. 830–842, Jan./Feb. 2022.
[22] X. Yi et al., "Transient synchronization stability analysis and enhancement of paralleled converters considering different current injection strategies," *IEEE Trans. Sustain. Energy*, vol. 13, no. 4, pp. 1957–1968, Oct. 2022.
[23] X. Fu, M. Huang, S. Pan, and X. Zha, "Cascading synchronization instability in multi-VSC grid-connected system," *IEEE Trans. Power Electron.*, vol. 37, no. 7, pp. 7572–7576, Jul. 2022.
[24] P. Bonckaert, P. De Maesschalck, T. S. Doan, and S. Siegmund, "Partial linearization for planar nonautonomous differential equations," *J. Differ. Equ.*, vol. 258, no. 5, pp. 1618–1652, 2015.

Xilin Li (Student Member, IEEE) was born in Wuhan, Hubei Province, China, in 1999. He received the B.Eng. degree major in electrical engineering and minor in computer science and technology in 2021 from Wuhan University, Wuhan, China, where he is currently working toward the Ph.D. degree in electrical engineering.

His research interests include the control and transient stability analysis of converter-based power systems.

Zhen Tian (Member, IEEE) received the B.S. degree in electrical engineering from Wuhan University, Wuhan, China, in 2014, and the Ph.D. degree in control science and engineering from Shanghai Jiao Tong University, Shanghai, China, in 2019.

During 2017–2019, he was a Visiting Scholar with the Department of Electrical and Computer Engineering, Illinois Institute of Technology, Chicago, USA. He was a Postdoctoral Fellow with the School of Electrical Engineering and Automation, Wuhan University, where he has been an Associate Research Fellow since 2022. His research interests mainly include modeling, control and stability analysis of renewable energy generation, microgrid, and power-electronics-enabled power systems.

Xiaoming Zha (Senior Member, IEEE) was born in Huaining, Anhui Province, China, in 1967. He received the B.S., M.S., and Ph.D. degrees in electrical engineering from Wuhan University, Wuhan, China, in 1989, 1992, and 2001, respectively.

From 2001 to 2003, he was a Postdoctoral Fellow with the University of Alberta, Canada. He has been a Faculty Member of Wuhan University since 1992, and became a Professor in 2003. He is currently the Deputy Dean with the School of Electrical Engineering, Wuhan University. His research interests include power electronic converter, the application of power electronics in smart grid and renewable energy generation, the analysis and control of microgrid, the analysis and control of power quality, and frequency control of high-voltage high-power electric motors.

Pengfei Sun was born in Zibo, Shandong, China, in 1997. He received the B.S. degree from Harbin University of Science and Technology, Harbin, China, in 2019, and the M.S. degree from Harbin Institute of Technology, Harbin, China, in 2021, both in electrical engineering. Since 2022, he has been working toward the Ph.D. degree in electrical engineering with Wuhan University, Harbin, China.

His current research interests include simultaneous wireless power and data transfer, modeling, and control of grid-tied converter.

Yufei Hu was born in Jianli, Hubei Province, China. He received the B.Eng. degree in electrical engineering in 2021 from Wuhan University, Wuhan, China, where he is currently working toward the M.Eng. degree in electrical engineering.

His current research interests include control and stability analysis of grid-integrated wind turbines

Meng Huang (Member, IEEE) received the B.Eng. and M.Eng. degrees from the Huazhong University of Science and Technology, Wuhan, China, in 2006 and 2008, respectively, and the Ph.D. degree from the Hong Kong Polytechnic University, Hong Kong, in 2013, all in electrical engineering.

He is currently an Associate Professor of the School of Electrical Engineering and Automation, Wuhan University, Wuhan, China. His research interests include nonlinear analysis of power converters and power electronics reliability.

Dr. Huang received the best paper award of the IEEE TRANSACTIONS ON POWER ELECTRONICS in 2016. He serves as the Guest Associate Editor for the IEEE JOURNAL OF EMERGING AND SELECTED TOPICS OF POWER ELECTRONICS, IEEE JOURNAL OF EMERGING AND SELECTED TOPICS OF CIRCUITS AND SYSTEMS, and an Associate Editor for the IEEE ACCESS.

Jianjun Sun (Member, IEEE) was born in 1975. He received the B.Eng., M.Eng., and Ph.D. degrees in electrical engineering from Wuhan University, Wuhan, China, in 1997, 2000, and 2007, respectively.

He is currently a Professor with the School of Electrical Engineering, Wuhan University, where he is also the Deputy Director of the Motor and Power Electronics Center. His current research interests include modeling and analysis of power electronic systems and microgrids.